Journal of Materials Chemistry A

Peculiarly Fast Li-ion Conduction Mechanism in a Succinonitrile-Based Molecular Crystal Electrolyte: A Molecular Dynamics Study

Journal:	*Journal of Materials Chemistry A*
Manuscript ID	TA-ART-04-2021-002809.R1
Article Type:	Paper
Date Submitted by the Author:	01-Jun-2021
Complete List of Authors:	Sasaki, Ryoma; Tokyo Institute of Technology, Department of Chemical Science and Engineering Moriya, Makoto; Shizuoka University, Department of Chemistry, Graduate School of Science Watanabe, Yuki; Tokyo Institute of Technology Nishio, Kazunori; Tokyo Institute of Technology, Chemical Science and Engineering Hitosugi, Taro; Tokyo Institute of Technology, Tateyama, Yoshitaka; National Institute for Materials Science, Center for Green Research on Energy and Environmental Materials (GREEN)

ARTICLE

Peculiarly Fast Li-ion Conduction Mechanism in a Succinonitrile-Based Molecular Crystal Electrolyte: A Molecular Dynamics Study

Received 00th January 20xx,
Accepted 00th January 20xx

DOI: 10.1039/x0xx00000x

Ryoma Sasaki,[*a,b] Makoto Moriya,[c,d] Yuki Watanabe,[a] Kazunori Nishio,[a] Taro Hitosugi,[a] and Yoshitaka Tateyama[*a,b]

$Li\{N(SO_2F)_2\}(NCCH_2CH_2CN)_2$ ($Li(FSA)(SN)_2$) molecular crystal has been experimentally reported as a promising solid electrolyte for all-solid-state Li-ion battery applications because of its high Li-ion conductivity of ca. 10^{-4} S cm^{-1} at room temperature and exceptionally low activation energy (E_a) of 28 kJ mol^{-1} [K. Tanaka *et al.*, *Nano Lett.*, 2020, **20**, 8200-8204]. However, the fast conduction mechanism remains unexplained because all the Li-ions are held in the crystal framework, and the distances between the constituent Li-ions are too long for hopping. Herein, molecular dynamics (MD) simulations were performed to clarify the mechanism of the extraordinarily fast Li-ion conduction in the succinonitrile (SN)-based molecular crystal. Atomistic MD revealed that Li-ion vacancies can exist stably in $Li(FSA)(SN)_2$ crystal and give rise to the one-dimensional Li-ion hopping pathway contrary to the conventional scenario in which the fast conduction is attributed to the three-dimensional pathway. The calculated E_a of 34 kJ mol^{-1} is in good agreement with the experimental value, which substantially supports the one-dimensional conduction. The low E_a is intimately connected with the motion of the SN molecules. Two SN molecules at the vacancy site change their conformation, following which one of the SN molecules creates an electronegative region, while the other one carries the adjacent Li-ion to the electronegative region by the swing motion. The insights on the behavior of organic moieties and Li-ion conduction obtained from this study will promote the development of highly conductive molecular crystals.

1 Introduction

All-solid-state Li-ion batteries have attracted considerable attention as next-generation power sources because of their high energy density and safety.[1–4] In these battery systems, the highly flammable conventional liquid electrolytes are replaced with safe solid-state electrolytes (SSEs). However, there are three key issues with SSEs that still need to be resolved including (1) poor conductivity, (2) high electrode/SSE interfacial resistance and poor adhesion to electrodes, and (3) low mechanical stability and deformability. Organic SSEs are intrinsically superior over inorganic SSEs in terms of the last two issues because they are mechanically soft and can better accommodate the electrode volume change during battery operation. Consequently, they have good contact with the electrode.[5–7] However, the low conductivity of organic SSEs is problematic for practical applications.

A reasonable approach for improving the conductivity of organic SSEs is to form an ordered phase with favorable ionic conduction pathways. Using this approach, inorganic ceramic ionic conductors such as $Li_{10}GeP_2S_{12}$ with high conductivity similar to those of liquid electrolytes,[8] have been developed. In this context, flexible organic molecular crystals (MCs) are expected to exhibit both good conductivity as well as good mechanical properties.[9] However, fabricating favorable conduction pathways is very difficult as evident from the low conductivity (on the order of 10^{-6} S cm^{-1} at room temperature) of most of the reported organic MCs, owing to the high activation energies(E_a) of these materials (40–100 kJ mol^{-1}).[10,11,20–28,12–19] Although $LiCl\{(CH_3)_2NCHO\}$ MC has good Li-ion conductivity (σ_{Li}) of 0.4×10^{-4} S cm^{-1} at 25°C, the high E_a of 81 kJ mol^{-1} limits its use at low temperatures.[26] Therefore, constructing the conduction pathway with low E_a is required for achieving the high σ_{Li} over a wide temperature range.

Recently, some of the authors have reported a new MC electrolyte, $Li\{N(SO_2F)_2\}(NCCH_2CH_2CN)_2$ ($Li(FSA)(SN)_2$), with high σ_{Li} of 1×10^{-4} S cm^{-1} at room temperature (transference number of Li-ion $t_{Li} = 0.95$) and outstandingly low E_a of 28 kJ mol^{-1}.[29] The low E_a of $Li(FSA)(SN)_2$ is comparable to those of most of the representative inorganic ceramic electrolytes such as the sulfide electrolyte, $Li_{10}GeP_2S_{12}$ (LGPS; 24 kJ mol^{-1})[8] and garnet-type electrolyte, $Li_7La_3Zr_2O_{12}$ (LLZO; 29–32 kJ mol^{-1}).[30,31] In the case of these inorganic ceramic electrolytes, the low E_a is

[a] School of Materials and Chemical Technology, Tokyo Institute of Technology, Tokyo 152-8552, Japan.
[b] Center for Green Research on Energy and Environmental Materials (GREEN) and International Center for Materials Nanoarchitectonics (MANA), National Institute for Materials Science (NIMS), Ibaraki 305-0044, Japan. E-mail: TATEYAMA.Yoshitaka@nims.go.jp
[c] Department of Science, Graduate School of Integrated Science and Technology, Shizuoka University, Shizuoka 422-8529, Japan.
[d] College of Science, Academic Institute, Shizuoka University, Shizuoka 422-8529, Japan.

† Electronic Supplementary Information (ESI) available: MSDs in Perfect-crystal mode, Li-vacancy model, FSA-vacancy model, and Li-interstitial model; details of the calculation of self-diffusion coefficient; details of Rigid dihedral FF and All-trans FF; chemical structure of fumaronitrile. See DOI: 10.1039/x0xx00000x

originated from (1) the partially filled interstitial Li-ion sites and (2) the short Li–Li distance. By contrast, in $Li(FSA)(SN)_2$ (**Fig.1**(a)), all the Li-ion sites are fully occupied and not interstitial because all the Li-ions are held in place by four succinonitrile (SN) groups as part of the Li–SN framework. Moreover, the minimum Li–Li distance in $Li(FSA)(SN)_2$ is 5.03Å, which is significantly longer than those in LGPS (2.4 Å) and LLZO (2.5 Å). To sum up, $Li(FSA)(SN)_2$ has neither partially occupied interstitial site nor short Li–Li distance. For these reasons, the unusually low E_a value in $Li(FSA)(SN)_2$ cannot be explained merely from the conventional viewpoint of the crystal structure. Therefore, understanding the peculiar conduction mechanism of $Li(FSA)(SN)_2$ is not only of practical importance, but is also of fundamental value.

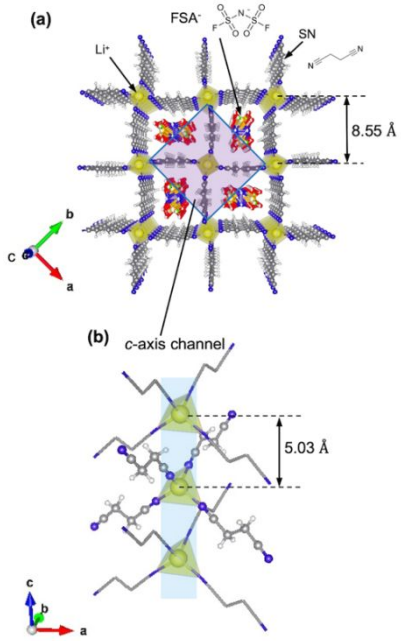

Fig. 1 (a) Crystal structure of $Li\{N(SO_2F)_2\}(NCCH_2CH_2CN)_2$ ($Li(FSA)(SN)_2$) reported by K. Tanaka *et al*.[29] (b) Stacked structure of Li-ions tetrahedrally coordinated with four SNs along the *c*-axis (FSA molecules are omitted for clarity). The Li-ion channel is formed along the *c*-axis

In this study, we investigated the Li-ion conduction mechanism in bulk $Li(FSA)(SN)_2$ MC using molecular dynamics (MD) simulations. As the conductivity has been linked with the defects in the previous literatures,[16,22,32–39] we first investigated the effect of removing a Li-ion from the Li–SN crystalline framework on the ordered structure of the material. Next, we calculated the mean-square displacements (MSDs) of ions in both the perfect and defective crystals to identify the most plausible conduction pathway. Furthermore, by analyzing a snapshot of Li-ion conduction, we inferred that the atomistic conduction mechanism involves trans-gauche isomerization and swing motion of the SN moiety. Based on this mechanism, the correlation between the trans-gauche flexibility and Li-ion conduction was demonstrated by MD as a virtual experiment using the devised force field parameters with the different torsional potential shape of the SN group. Finally, we have suggested a new guideline for enhancing the conductivity of SN-based crystals.

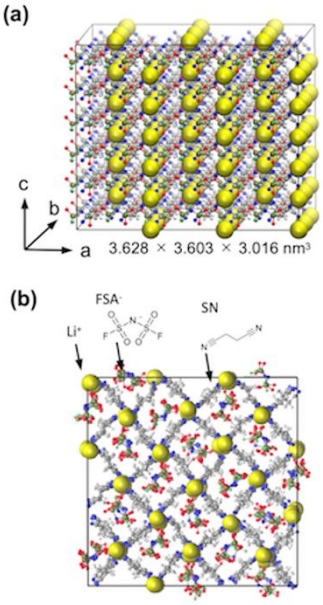

Fig. 2 (a) Initial structure of $Li(FSA)(SN)_2$, which was implemented as a 3 × 3 × 6 supercell ($Li_{108}FSA_{108}SN_{216}$). (b) Equilibrated structure at 300 K and 1 bar.

2 Computational methods

All the MD and quantum chemical calculations were performed using GROMACS 2016.6[40] and Gaussian 16 Revision C.01,[41] respectively. We used the second generation of the general AMBER force field (GAFF2)[42] for the MD calculations . To obtain the atomic partial charges, geometry optimization was carried out at the ωB97X-D/6-311+G(d) level, and the restrained electrostatic potential (RESP) charges[43] were obtained at the HF/6-311+G(d) level. A charge scaling factor of 0.8 was used to correct the overestimation in the electrostatic point charges of the ionic species.[44] A cutoff radius of 1.2 nm was used for the Lennard-Jones and screened real-space Coulombic interactions. The particle–particle particle-mesh (pppm) method[45] was employed to compute the long-range Coulombic interactions. The LINCS algorithm[46] was used to keep all the bond lengths fixed at their equilibrium values, and a time step of 2 fs was employed.

The initial structure was constructed in a 3 × 3 × 6 supercell (**Fig. 2**(a); 108 Li, 108 FSA, and 216 SN moieties in 3.628 × 3.603 × 3.016 nm^3) based on the X-ray crystalline structure experimentally determined at 230 K.[29] The system was equilibrated for 600 ns using an isothermal–isobaric (*NpT*) ensemble using a Nosé–Hoover thermostat and Parrinello–

Rahman barostat at a pressure of 1 bar and temperature range of 270−420 K, to check whether the crystalline structure was retained. As shown in **Fig. 2**(b), the crystalline structure was retained at 300 K, which was lower than the melting point. The production run was performed under a canonical (*NVT*) ensemble using a Nosé-Hoover thermostat at the *NpT*-equilibrated density. To investigate the effect of an ionic vacancy, we removed one ionic species and redistributed its charge to the other ionic species to satisfy charge neutrality.[47,48]

3 Results and discussions

3.1 Crystal structure

The *NpT* calculations were performed using the Perfect-crystal (108 Li + 108 FSA + 216 SN) and Li-vacancy (107 Li + 108 FSA + 216 SN) models at 230 K, which corresponds to the temperature at which the experimental X-ray diffraction (XRD) measurements were carried out.[29] The MC densities obtained (Perfect-crystal model: 1488 kg m^{-3} and Li-vacancy model: 1486 kg m^{-3}) were 6% lower than the experimental value[29] (1579 kg m^{-3}). To validate the FF used, the melting point of the MC was estimated, by using the point at which the density as a function of temperature changes sharply in the *NpT* simulations. **Fig. 3** shows the relationship between temperature and densities as well as the experimental differential scanning calorimetry (DSC) curve.[29] The melting point obtained from the Li-vacancy model (ca. 325 K) was lower than that obtained from the Perfect-crystal model (ca. 370 K) because of the loss of Li-ions from the framework in the former case. However, even this reduced melting point was comparable to the experimental value (ca. 335 K). Hence, the calculated macroscopic physical properties, i.e., density and melting temperature, were comparable with the experimental values. Furthermore, the results demonstrate that the Li–SN crystalline structure was retained even when a Li-ion was removed from the framework.

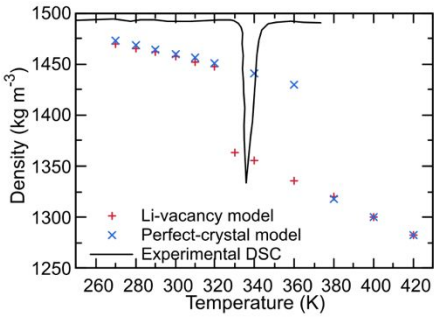

Fig. 3 *NpT*-equilibrated densities of the Li-vacancy and Perfect-crystal models, compared with the experimental DSC curves[29] for $Li(FSA)(SN)_2$. The initial structure of all the points is crystalline.

We investigated the structural changes in the Li–SN framework (**Fig. 1**) arising from the removal of one Li-ion in the Li-vacancy model. **Fig. 4**(a) shows the radial distribution functions and coordination numbers (CNs) of Li-ions to the nitrogen atoms of SN in the *c*-axis channel (**Fig. 1**(b)) with and without Li-ion vacancies. The CN of the first solvation shell in the channel containing vacancies was higher than that in the channel without a Li-ion vacancy. This increase in CN was a consequence of the excess SN caused by the removal of the Li-ion. The excess SNs were coordinated to the Li-ion next to the vacancy, as the SNs fluctuated between the trans and gauche conformations (**Fig. 4**(b)). Thus, the Li–SN framework containing one Li-ion vacancy remained stable because of the excess SN coordination to the adjacent Li-ions.

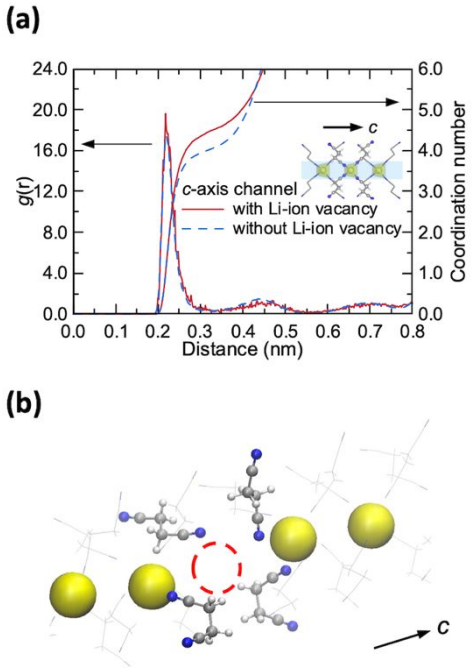

Fig. 4 (a) Radial distribution functions and coordination numbers for the Li-ions in the *c*-axis channel with and without a Li-ion vacancy, towards the nitrogen atoms in SN. (b) Snapshot showing the coordination of excess SNs (cyan-colored molecules) to the adjacent Li-ion.

3.2 Effect of Li-ion vacancy on Li-ion diffusion

We calculated the MSDs of the constituents in both the Li-vacancy and Perfect-crystal models at 300 K, and the results are shown in **Fig. 5**(a). In the Perfect-crystal model, all the slopes of the MSDs were almost plateau with time, exhibiting no ionic diffusion. However, in the Li-vacancy model (**Fig. 5**(b)), the slope of the MSDs of Li-ions along the *c*-axis increased dramatically, whereas that of the FSA ion remained almost plateau. The selective diffusion of Li-ions indicates a t_{Li} of 1, which is consistent with the experimental t_{Li} value of 0.95.[29] We also compared the MSDs of Li-ions in the defective *c*-axis channel with those of the other Li-ions (**Fig. 5**(c)). The results show that the Li-ions in the defective *c*-axis channel diffused, while those in the *c*-axis channel without a vacancy did not diffuse. In addition, we investigated the effect of FSA vacancies and excess Li in the interstitial sites on the Li-ion diffusion (**Section S1**) and

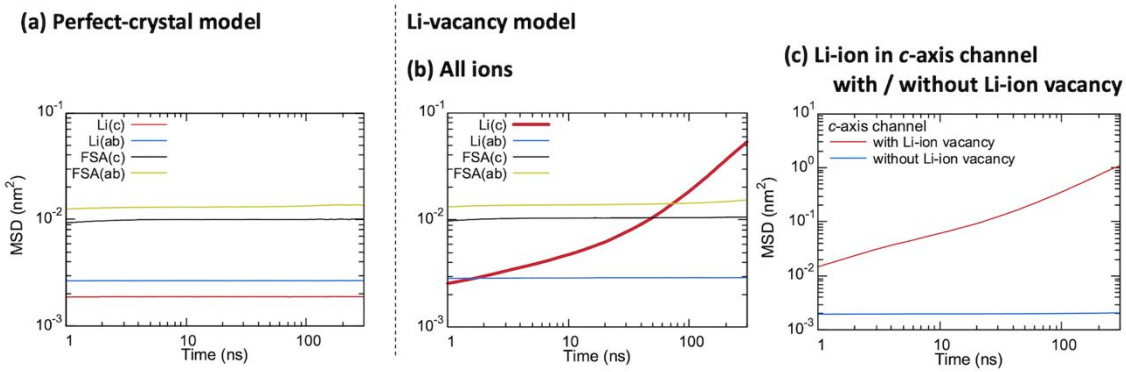

Fig. 5 Comparison of the mean squared displacements (MSDs) of all the ionic species between the (a) Perfect-crystal model and (b) Li-ion vacancy model. (c) MSDs of all the Li-ions in *c*-axis channels with and without one Li-ion vacancy in the Li-ion vacancy model.

found that the Li-ions did not diffuse to the same extent in these cases (**Fig. S1**(b)). Thus, our calculations demonstrated that the conduction of Li(FSA)$(SN)_2$ is anisotropic, and is promoted by the Li-ion vacancies in the defective *c*-axis channels. This is a revelation in contrast to the conventional aspect that higher ionic conductivity is usually related to the presence of three-dimensional conduction pathways.

We then calculated the Li-ion conductivity along the *c*-axis using the Li-vacancy model (**Fig. 6**), which is suggested to be the most plausible Li conduction scheme in the above analysis (**Fig. 5**). The conductivity is calculated with the Nernst-Einstein relationship: $\sigma_{Li} = n_{Li}F^2D_{Li}/(VRT)$, where n_{Li} is the number of the Li-ion carriers in the defective *c*-axis channel (5 atoms in this study), F is Faraday's constant, D_{Li} is the self-diffusion coefficient of the conductive Li-ion carriers, and V is the cell volume, R is the universal gas constant, and T is the temperature. The diffusion coefficient value was determined from the slope of the MSDs (**Section S2**). The Li-ion conductivity at room temperature was estimated to be approximately 1×10^{-5} S cm^{-1}, which is reasonably consistent with the experimental value, given the uncertainty of the density of Li-ion vacancy. In addition, the activation energy for Li-ion conduction along the *c*-axis was estimated using the relationship between temperature and calculated conductivity (**Fig. 6**) and was found to be 34 kJ mol^{-1}, which is in good agreement with the experimentally determined value of 28 kJ mol^{-1}. These results strongly support that the primary mode of diffusion for the Li-ions involves hopping along the *c*-axis promoted by the Li-ion vacancies.

Selected snapshots of Li-ion hopping stages in the Li-vacancy model as well as the perfect crystalline structure are presented in **Fig. 7**. **Fig. 7**(a) shows two ligand SN entities associated with the Li-ion at the vacancy site, indicated by the purple molecules (SN-1 and SN-2), isomerized from the original trans conformation (**Fig. 7**(upper)) to gauche one to coordinate to the adjacent Li ion. Next, the purple SNs isomerized from the gauche to trans conformation as shown in **Fig. 7**(b). Following the isomerization, the swing motion of purple SN-1 carried the Li-ion to the electronegative region created by the trans conformation of the SN-2 (**Fig. 7**(b) → (c)). Finally, the newly generated excess SN (orange molecules) isomerized from the trans to gauche conformation (**Fig. 7**(d)). Thus, the important motions for Li-ion hopping include the gauche→trans isomerization of the excess SN and the swing motion of SN. Interestingly, this mechanism shows that the Li-ions constructing the ordered framework also act as transport carriers.

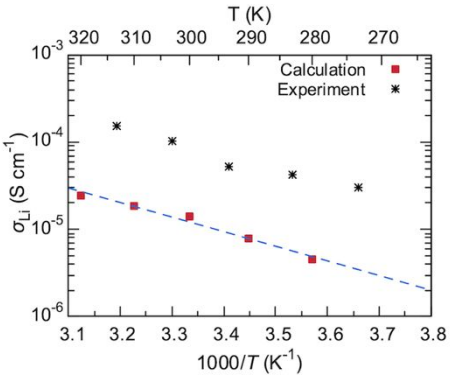

Fig. 6 Plot of calculated Li-ion conductivity along the *c*-axis (σ_{Li}, in S cm^{-1}) vs 1000 T^{-1} (K^{-1}) from the Li-vacancy model and experimental conductivity.[29]

3.3 Relationship between the flexibility of SNs in the trans-gauche isomerism and Li-ion diffusion

As mentioned above, the flexibility of the trans-gauche isomerism of SN is a key factor for Li-ion hopping. In this subsection, we clarify the correlation between the rotational profile of the central C-C bond of SN and Li-ion diffusivity. Furthermore, we propose a new method for increasing the conductivity of SN-based ionic conductors.

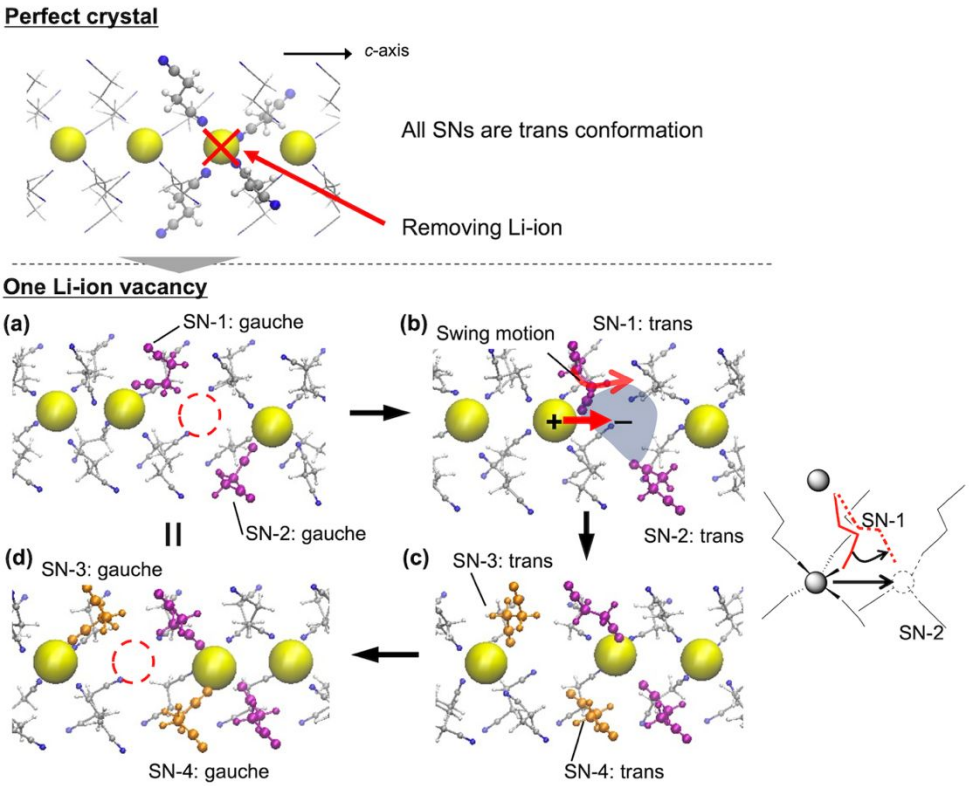

Fig. 7 Snapshots of the perfect crystalline structure (upper) and Li-ion hopping cycles in the Li-ion vacancy model (lower). FSA ions are omitted for simplicity. Perfect crystal→(a): trans→gauche isomerization (t→g) of the excess SNs (SN-1 and SN-2) at the Li-ion vacancy. (a)→(b): g→t conformation changes of SN-1 and SN-2. (b)→(c): SN-1 carries the Li-ion into the electronegative region involving SN-2. (c)→(d): t→g isomerization of the new excess SNs (SN-3 and SN-4).

To investigate the correlation between the torsional potential of SN and Li-ion diffusion, we prepared two FFs: (1) Rigid dihedral FF and (2) All-trans FF. Further details of the two FFs are provided in the **Section S3**. **Fig. 8**(a) shows the rotational potentials as a function of the dihedral angle of the NC-C-C-CN of SN. Rigid dihedral FF exhibited a larger activation energy for the isomerization from gauche to trans conformation (E_a(g→t)) compared to GAFF2. In the All-trans FF, the dihedral angle of the NC-C-C-CN is kept trans, while the swing motion is allowed. Based on the results obtained using these two modified FFs, the relationship between trans-gauche flexibility and Li-ion diffusion was clarified.

Based on the Li-ion diffusion mechanism deduced above (**Fig. 7**), the large E_a(g⟶t) (Rigid-dihedral FF) is expected to prevent SN isomerization from the gauche to trans conformation, which leads to a decrease in the self-diffusion coefficient. **Fig. 8**(b) shows that the MSD of the rigid dihedral FF is lower than that of GAFF2, which supports the conduction mechanism that is presented here.

With the All-trans FF, the first SN isomerization process (**Fig. 7**(a)→(b)) is not necessary because the SNs present around the Li-ion vacancy exhibit a trans conformation. Therefore, the activation energy required for isomerization is eliminated, and Li-ion hopping is expected to be more facile. To validate this hypothesis, we calculated the MSD using the All-trans FF (**Fig. 8**(b)). The self-diffusion coefficient in the case of All-trans FF (6.8×10^{-8} cm^2 s^{-1}) was 3.6 times higher than that of GAFF2 (1.9×10^{-8} cm^2 s^{-1}). This new insight obtained by focusing on the rotational motion of the organic molecules around Li-ion vacancies is useful for designing highly conductive organic solid electrolytes.

Finally, we propose a methodology for enhancing Li-ion conductivity. As shown in **Fig. 8**(b), Skipping the isomerization process from the gauche to the trans conformation (Fig. 7(a)→(b)) enhanced the Li-ion diffusion. On the basis of these results, we suggest that replacing SN with fumaronitrile NC–CH=CH–CN (**Fig. S5**) is likely to be effective in further improving the Li-ion conductivity because fumaronitrile always has a trans conformation due to the presence of the central double bond, which can skip the g→t isomerization process (Fig. 7(a)→(b)), but still allow the swing motion. While some experimental studies have shown that adding various nitriles with the C–C single bond to the SN-based ionic conductor is effective for increasing ionic conduction,[49,50] fumaronitrile with the C=C double bond can be utilized as a novel dopant in the form of $Li(FSA)_2(SN)_{2-x}(fumaronitrile)_x$.

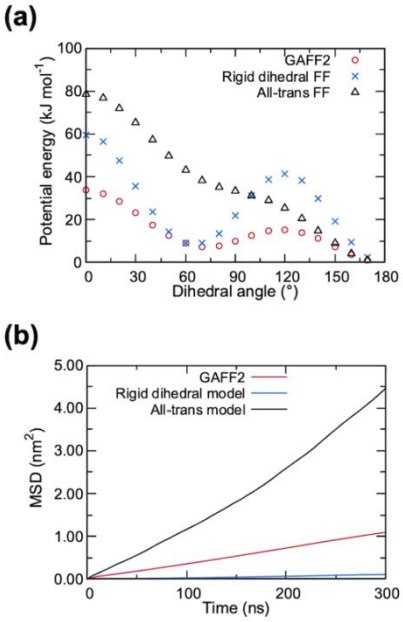

Fig. 8 (a) Torsional potential energy of the central C-C bond in SN. The red circles, blue crosses, and black triangles represent the results obtained using GAFF2, Rigid dihedral FF, and All-trans FF, respectively. (b) Comparison of the MSD of Li-ion obtained by normal GAFF2 with the Rigid dihedral and All-trans models.

4 Conclusion

We theoretically investigated the mechanism of the peculiarly fast Li-ion conduction in the $Li(FSA)(SN)_2$ MCs by MD simulations. We found that the presence of a Li-ion vacancy gives rise to a one-dimensional fast Li-ion conduction pathway. It should be emphasized that even though Li-ions are essential components of the Li–SN framework, the removal of Li-ions had little effect on the stability of the crystalline structure since the SNs adjust by coordinating to the adjacent Li-ions when there is a vacancy present in the framework.

In the conduction pathway, Li-ion hopping occurs via two processes: (1) flexible gauche → trans isomerization of two SNs at the Li-ion vacancy and (2) swing motion of one SN holding Li-ions towards the vacancy. This mechanism shows that the Li-ions constructing the crystalline framework can also act as transport carriers, which was thoroughly validated by the devised FFs with the different trans-gauche flexibility of SN. Finally, we have proposed a new guideline for enhancing the conductivity of the MC by doping with fumaronitrile ($Li(FSA)_2(SN)_{2-x}$(fumaronitrile)$_x$), in which the process of gauche → trans isomerization will be eliminated. The present conduction mechanism, which focuses on the conformational behavior of organic moieties around the Li-ion vacancy, enables the design of highly conductive MCs.

Conflicts of interest

There are no conflicts to declare.

Acknowledgements

R.S. acknowledges the financial support for JSPS Research Fellowships for Young Scientists (Grant number: JP21J12566). This work was also supported in part by JSPS KAKENHI (Grant Number: JP19H05815 and JP18H03876), JST-CREST (Grant number: JPMJCR20T3), and MEXT as part of the "Program for Promoting Research on the Supercomputer Fugaku (Fugaku Battery & Fuel Cell Project), grant number JPMXP1020200301". The calculations were carried out on the supercomputers at the National Institute for Materials Science (NIMS) and the TSUBAME 3.0 at the Tokyo Institute of Technology (the resource of the TSUBAME 3.0 is partially supported by the MEXT Project of the Tokyo Tech Academy for Convergence of Materials and Informatics (TAC-MI)). In this research, the computational resources of the supercomputers at the RIKEN and HPCI Systems were also used, through the HPCI System Research Projects (project IDs: hp200131 and hp210173).

References

1 A. Manthiram, X. Yu and S. Wang, *Nat. Rev. Mater.*, 2017, **2**, 16103.
2 C. Sun, J. Liu, Y. Gong, D. P. Wilkinson and J. Zhang, *Nano Energy*, 2017, **33**, 363–386.
3 R. Chen, Q. Li, X. Yu, L. Chen and H. Li, *Chem. Rev.*, 2020, **120**, 6820–6877.
4 Q. Zhao, S. Stalin, C.-Z. Zhao and L. A. Archer, *Nat. Rev. Mater.*, 2020, **5**, 229–252.
5 A. Arya and A. L. Sharma, *Ionics*, 2017, **23**, 497–540.
6 T. Liu, Y. Zhang, R. Chen, S. X. Zhao, Y. Lin, C. W. Nan and Y. Shen, *Electrochem. commun.*, 2017, **79**, 1–4.
7 X. Wang, R. Kerr, F. Chen, N. Goujon, J. M. Pringle, D. Mecerreyes, M. Forsyth and P. C. Howlett, *Adv. Mater.*, 2020, **32**, 1905219.
8 N. Kamaya, K. Homma, Y. Yamakawa, M. Hirayama, R. Kanno, M. Yonemura, T. Kamiyama, Y. Kato, S. Hama, K. Kawamoto and A. Mitsui, *Nat. Mater.*, 2011, **10**, 682–686.
9 M. Moriya, *Sci. Technol. Adv. Mater.*, 2017, **18**, 634–643.
10 T. Nakamura, T. Akutagawa, K. Honda, A. E. Underhill, A. T. Coomber and R. H. Friend, *Nature*, 1998, **394**, 159–162.
11 R. E. A. Dillon and D. F. Shriver, *Chem. Mater.*, 1999, **11**, 3296–3301.
12 R. E. A. Dillon, C. L. Stern and D. F. Shriver, *Chem. Mater.*, 2001, **13**, 2516–2522.
13 G. S. MacGlashan, Y. G. Andreev and P. G. Bruce, *Nature*, 1999, **398**, 792–794.
14 Z. Gadjourova, Y. G. Andreev, D. P. Tunstall and P. G. Bruce, *Nature*, 2001, **412**, 520–523.
15 Z. Gadjourova, D. Martín y Marero, K. H. Andersen, Y. G. Andreev and P. G. Bruce, *Chem. Mater.*, 2001, **13**, 1282–1285.
16 A. M. Christie, S. J. Lilley, E. Staunton, Y. G. Andreev and P.

G. Bruce, *Nature*, 2005, **433**, 50–53.
17 C. Zhang, E. Staunton, Y. G. Andreev and P. G. Bruce, *J. Am. Chem. Soc.*, 2005, **127**, 18305–18308.
18 S. J. Lilley, Y. G. Andreev and P. G. Bruce, *J. Am. Chem. Soc.*, 2006, **128**, 12036–12037.
19 C. Zhang, Y. G. Andreev and P. G. Bruce, *Angew. Chem., Int. Ed.*, 2007, **46**, 2848–2850.
20 C. Zhang, D. Ainsworth, Y. G. Andreev and P. G. Bruce, *J. Am. Chem. Soc.*, 2007, **129**, 8700–8701.
21 C. Zhang, S. Gamble, D. Ainsworth, A. M. Z. Slawin, Y. G. Andreev and P. G. Bruce, *Nat. Mater.*, 2009, **8**, 580–584.
22 M. Moriya, H. Kitaguchi, E. Nishibori, H. Sawa, W. Sakamoto and T. Yogo, *Chem. -Eur. J.*, 2012, **18**, 15305–15309.
23 M. Moriya, D. Kato, Y. Hayakawa, W. Sakamoto and T. Yogo, *Solid State Ionics*, 2016, **285**, 29–32.
24 M. Moriya, K. Nomura, W. Sakamoto and T. Yogo, *CrystEngComm*, 2014, **16**, 10512–10518.
25 M. Moriya, D. Kato, W. Sakamoto and T. Yogo, *Chem. -Eur. J.*, 2013, **19**, 13554–13560.
26 P. R. Chinnam, R. N. Clymer, A. A. Jalil, S. L. Wunder and M. J. Zdilla, *Chem. Mater.*, 2015, **27**, 5479–5482.
27 B. Fall, A. A. Jalil, M. Gau, S. Chereddy, M. J. Zdilla, S. L. Wunder and P. R. Chinnam, *Ionics*, 2018, **24**, 343–349.
28 O. Yui and M. Moriya, *Crystals*, 2019, **9**, 567.
29 K. Tanaka, Y. Tago, M. Kondo, Y. Watanabe, K. Nishio, T. Hitosugi and M. Moriya, *Nano Lett.*, 2020, **20**, 8200–8204.
30 R. Murugan, V. Thangadurai and W. Weppner, *Angew. Chem., Int. Ed.*, 2007, **46**, 7778–7781.
31 J. Sakamoto, E. Rangasamy, H. Kim, Y. Kim and J. Wolfenstine, *Nanotechnology*, 2013, **24**, 424005.
32 R. Cheerla and M. Krishnan, *Macromolecules*, 2016, **49**, 700–707.
33 R. Cheerla and M. Krishnan, *Polymer (Gu.*, 2018, **155**, 136–145.
34 P. Prakash, J. Aguirre, M. M. Van Vliet, P. R. Chinnam, D. A. Dikin, M. J. Zdilla, S. L. Wunder and A. Venkatnathan, *J. Mater. Chem. A*, 2018, **6**, 4394–4404.
35 B. Fall, P. Prakash, M. R. Gau, S. L. Wunder, A. Venkatnathan and M. J. Zdilla, *Chem. Mater.*, 2019, **31**, 8850–8863.
36 F. Chen, S. W. de Leeuw and M. Forsyth, *J. Phys. Chem. Lett.*, 2013, **4**, 4085–4089.
37 M. Forsyth, F. Chen, L. A. O'Dell and K. Romanenko, *Solid State Ionics*, 2016, **288**, 160–166.
38 F. Chen, J. M. Pringle and M. Forsyth, *Chem. Mater.*, 2015, **27**, 2666–2672.
39 J. B. Hooper and O. Borodin, *Phys. Chem. Chem. Phys.*, 2010, **12**, 4635–4643.
40 D. Van Der Spoel, E. Lindahl, B. Hess, G. Groenhof, A. E. Mark and H. J. C. Berendsen, *J. Comput. Chem.*, 2005, **26**, 1701–1718.
41 M. J. Frisch, G. W. Trucks, H. B. Schlegel, G. E. Scuseria, M. A. Robb, J. R. Cheeseman, G. Scalmani, V. Barone, G. A. Petersson, H. Nakatsuji, X. Li, M. Caricato, A. V. Marenich, J. Bloino, B. G. Janesko, R. Gomperts, B. Mennucci, H. P. Hratchian, J. V. Ortiz, A. F. Izmaylov, J. L. Sonnenberg, D. Williams-Young, F. Ding, F. Lipparini, F. Egidi, J. Goings, B. Peng, A. Petrone, T. Henderson, D. Ranasinghe, V. G. Zakrzewski, J. Gao, N. Rega, G. Zheng, W. Liang, M. Hada, M. Ehara, K. Toyota, R. Fukuda, J. Hasegawa, M. Ishida, T. Nakajima, Y. Honda, O. Kitao, H. Nakai, T. Vreven, K. Throssell, J. Montgomery, J. A., J. E. Peralta, F. Ogliaro, M. J. Bearpark, J. J. Heyd, E. N. Brothers, K. N. Kudin, V. N. Staroverov, T. A. Keith, R. Kobayashi, J. Normand, K. Raghavachari, A. P. Rendell, J. C. Burant, S. S. Iyengar, J. Tomasi, M. Cossi, J. M. Millam, M. Klene, C. Adamo, R. Cammi, J. W. Ochterski, R. L. Martin, K. Morokuma, O. Farkas, J. B. Foresman and D. J. Fox, 2016.
42 D. A. Case, I. Y. Ben-Shalom, S. R. Brozell, D. S. Cerutti, T. E. Cheatham III, V. W. D. Cruzeiro, T. A. Darden, R. E. Duke, D. Ghoreishi, M. K. Gilson, H. Gohlke, A. W. Goetz, D. Greene, R. Harris, N. Homeyer, Y. Huang, S. Izadi, A. Kovalenko, T. Kurtzman, T. S. Lee, S. LeGrand, P. Li, C. Lin, J. Liu, T. Luchko, R. Luo, D. J. Mermelstein, K. M. Merz, Y. Miao, G. Monard, C. Nguyen, H. Nguyen, I. Omelyan, A. Onufriev, F. Pan, R. Qi, D. R. Roe, A. Roitberg, C. Sagui, S. Schott-Verdugo, J. Shen, C. L. Simmerling, J. Smith, R. SalomonFerrer, J. Swails, R. C. Walker, J. Wang, H. Wei, R. M. Wolf, X. Wu, L. Xiao, D. M. York and P. A. Kollman, 2018.
43 C. I. Bayly, P. Cieplak, W. D. Cornell and P. A. Kollman, *J. Phys. Chem.*, 1993, **97**, 10269–10280.
44 K. G. Sprenger, V. W. Jaeger and J. Pfaendtner, *J. Phys. Chem. B*, 2015, **119**, 5882–5895.
45 R. W. Hockney and J. W. Eastwood, *Computer Simulation Using Particles*, McGraw-Hill International Book Co., New York, 1981.
46 B. Hess, H. Bekker, H. J. C. Berendsen and J. G. E. M. Fraaije, *J. Comput. Chem.*, 1997, **18**, 1463–1472.
47 J. Habasaki and K. L. Ngai, *J. Electroceramics*, 2015, **34**, 43–56.
48 T. Oda and S. Tanaka, *J. Nucl. Mater.*, 2009, **386–388**, 1087–1090.
49 K. Geirhos, P. Lunkenheimer, M. Michl, D. Reuter and A. Loidl, *J. Chem. Phys.*, 2015, **143**, 081101.
50 D. Reuter, P. Lunkenheimer and A. Loidl, *J. Chem. Phys.*, 2019, **150**, 244507.